# Nanoelectronics and Its New Materials – A NEW ERA OF NANOSCIENCE

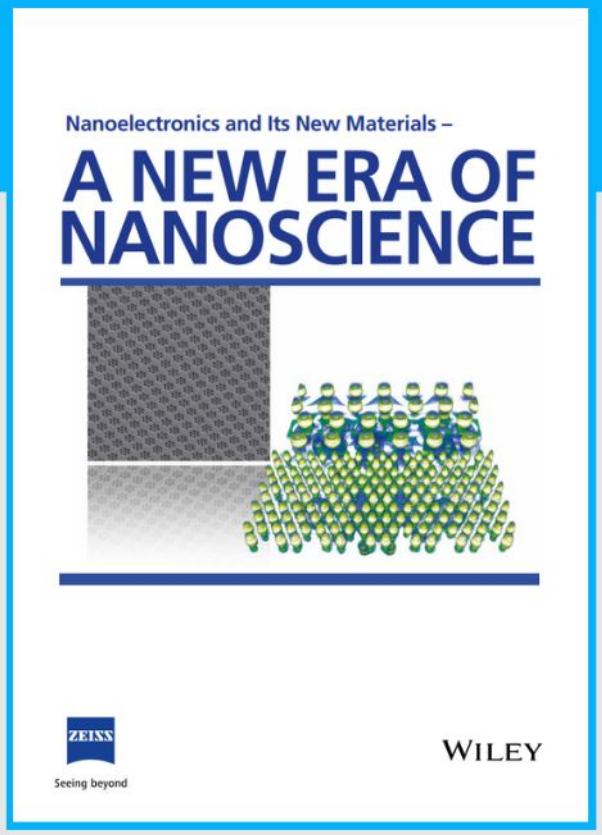


**Discover the recent advances in electronics research and fundamental nanoscience.**

Nanotechnology has become the driving force behind breakthroughs in engineering, materials science, physics, chemistry, and biological sciences. In this compendium, we delve into a wide range of novel applications that highlight recent advances in electronics research and fundamental nanoscience. From surface analysis and defect detection to tailored optical functionality and transparent nanowire electrodes, this eBook covers key topics that will revolutionize the future of electronics.

To get your hands on this valuable resource and unleash the power of nanotechnology, simply download the eBook now. Stay ahead of the curve and embrace the future of electronics with nanoscience as your guide.

ZEISS

Seeing beyond

WILEY

ADVANCED FUNCTIONAL MATERIALS
www.afm-journal.de

# Molecular Auxetic Polymer of Intrinsic Microporosity via Conformational Switching of a Cavitand Crosslinker

*Francesca Portone, Mattia Amorini, Matteo Montanari, Roberta Pinalli, Alessandro Pedrini, Roberto Verucchi, Roberto Brighenti, and Enrico Dalcanale**

**Auxetics are materials characterized by a negative Poisson's ratio (NPR), an uncommon mechanical behavior corresponding to a transversal deformation tendency opposite to the traditional materials. Here, the first example of a synthetic molecular auxetic polymer obtained by embedding a conformationally expandable cavitand as a crosslinker into a rigid polymer of intrinsic microporosity (PIM) is presented. The rigidity and microporosity of the polymeric matrix are pivotal to maximizing the expansion effect of the cavitand that, under mechanical stress, can assume two different conformations: a compact vase one and an extended kite form. The auxetic behavior and the corresponding NPR of the proposed material is predicted by a specific micromechanical model that considers the cavitand volume expansion ratio, the fraction of the cavitand crosslinker in the polymer, and the mechanical characteristics of the polymer backbone. The reversible auxetic behavior of the material is experimentally verified via the digital image correlation technique performed during the mechanical tests on films obtained by blending the auxetic crosslinked polymer with pristine PIM. Two specific control experiments prove that the mechanically driven conformational expansion of the cavitand crosslinker is the sole responsible for the observed NPR of the polymer.**

## 1. Introduction

Auxetics[1,2] are intriguing materials characterized by the counterintuitive property of lateral expansion upon longitudinal stretching, corresponding to a Negative Poisson's Ratio (NPR).[3] Most current synthetic auxetic materials, whose authenticity is triggered by the deformation of their meso/macroscopic structure, are discontinuous at the nanoscale and expand only when stretched in a particular direction, severely limiting their use in applications requiring a 3D mechanical response. At the macroscale, the auxetic property is usually obtained through foams having a particular architectural structure[4] or with so-called metamaterials, constituted by elements arranged in repeated patterns, whose properties depend on their geometrical lattice arrangement rather than on the properties of the base material.[5] Molecular auxetics overcome the limits of artificial auxetic metamaterials in terms of desired mechanical responses to multidirectional external loads, and allow tuning indentation stiffness, shear, fracture, and strength resistance. The major unresolved issue in auxetics is represented by the synthesis of isotropic and continuous (in a wide range of length scales) auxetic materials. This can be achieved by operating at the molecular level, since foams, metamaterials, and related structures are typically discontinuous at the mesoscale, leading to materials characterized by porosity-related weakening. As an alternative, continuous composites with properly organized soft or hard inclusions have been shown to be auxetic.[6,7]

The first theoretical model of an isotropic and thermodynamically stable molecular auxetic was published in 1987 by Wojciechowski,[8] foreseeing a NPR for a planar (2D) model of hard cyclic hexamers.[9] Afterward, inspired by macroscopic re-entrant honeycomb and rotating triangle structures, molecular auxetic behavior has been theoretically predicted for a variety of molecular networks constituted by "twisted-chain" polyacetylenes,[10] crosslinked rigid polyphenylacetylenes,[11] calix[4]arene-based polymeric network[12] and prismane-based molecular rods.[13] However, the synthesis of such precisely arranged, highly crosslinked structures revealed to be unfeasible so far. As an alternative, Griffin prepared main-chain liquid crystalline elastomers with bulky rigid laterally attached rods,

F. Portone, M. Amorini, R. Pinalli, A. Pedrini, E. Dalcanale
Department of Chemistry
Life Sciences and Environmental Sustainability and INSTM UdR Parma
University of Parma
Parco Area delle Scienze 17/A, Parma 43124, Italy
E-mail: enrico.dalcanale@unipr.it
M. Montanari, R. Brighenti
Department of Engineering & Architecture
University of Parma
Parco Area delle Scienze 181/A, Parma 43124, Italy
R. Verucchi
IMEM-CNR
Institute of Materials for Electronics and Magnetism
Trento unit, Via alla Cascata 56/C –, Trento 318123, Italy

The ORCID identification number(s) for the author(s) of this article can be found under https://doi.org/10.1002/adfm.202307605



**DOI: 10.1002/adfm.202307605**

susceptible to force-induced rotation upon stretching.[14] The interchain distance of the polymeric chains in the oriented nematic phase should increase in a direction perpendicular to the applied force. Even if a small increase in the interchain distance has been observed by X-ray scattering,[15] the reported system failed to evidence an auxetic behavior. More recently, auxetic 2D protein crystals, in which different conformational states of the self-assembled structures were obtained, have been proposed.[16]

In 2018 the first synthetic molecular auxetic was described by Gleeson et al.[17] It is a nematic liquid crystal elastomer (LCE), whose auxeticity is triggered by a negative ordering of the LCE backbone taking place beyond a given threshold strain. The anisotropic nature of LCEs allows for a NPR in one transverse axis provided that the other transverse axis has a positive PR, thus conserving volume. When the auxetic behavior occurs in only one axis, the corresponding material has been defined as partial auxetic.[18] Therefore the LCE is a partial auxetic.[19]

The absence of workable solutions to the synthesis of intrinsic molecular auxetics calls for a different approach to the problem. Here we report an unprecedented solution based on a conformationally expandable component called quinoxaline cavitand[20] inserted in a rigid polymer of intrinsic microporosity (PIM).

Cavitands were originally designed as molecular receptors.[21] More recently, cavitands' molecular recognition properties have been exploited as key components in supramolecular polymers[22,23] and molecular grippers.[24] Quinoxaline cavitands have the peculiar ability to switch between two well-defined conformations: a compact one, called a vase, and an extended one named a kite.[25] The vase-kite interconversion has been extensively investigated in solution via different stimuli, such as pH,[26,27] temperature,[25] metal coordination,[28,29] and redox.[24] density functional theory (DFT) calculations estimate the energy barrier for the interconversion between the two forms in 7.6 kcal $mol^{-1}$ and predict that the vase form is by 3.2 kcal $mol^{-1}$ more stable than the kite form.[30] All intermediate conformations are energetically disfavored, therefore only these two discrete conformers are observed. The vase-to-kite switch is characterized by a large dimensional expansion of the molecule, driven by the lateral opening of its four wings. Thanks to their two discrete conformational states, cavitands provide the desired kinematic response to induce NPR in PIMs. Preliminary studies carried out on polyurethane specimens cross-linked with quinoxaline cavitands evidenced the mechanically triggered vase-to-kite switching of a fraction of cavitands through the appearance of a diagnostic band of the kite conformer both in UV and fluorescence spectra.[31]

PIMs are a unique class of microporous materials containing a continuous network of interconnected intermolecular voids <2 nm in width,[32] widely used as membranes for gas separation.[33] PIMs are a special class of polymers, which form microporous solids because their conformationally rigid and contorted macromolecular chains do not efficiently pack in the solid state. Their intrinsic rigidity is the key ingredient to translate the mechanically driven conformational switch of cavitands into an auxetic behavior, by avoiding that the molecular expansion could be absorbed or heavily attenuated by local re-arrangements of the polymer backbone.

## 2. Results and Discussion

### 2.1. Theoretical Prediction of the Auxetic Behavior

We define "auxeton" as the cavitand expandable unit embedded in the **PIM1** polymer network. **Figure 1**a shows the proposed auxeton in the vase and kite conformers, considering as expandable wings the four planar panels resulting from the reaction of the crosslinking unit $\mathbf{C_V8H}$ (Scheme S2, Supporting Information and **Figure 2**a) with **PIM1** monomers up to the first spirobiindane contortion site (red and green fragments in Figure 1b). The two structures have been optimized via molecular mechanics calculations using the geometrical parameters obtained by the crystal structures of the two related cavitands as a base.[34,35] The linear conformational expansion in one direction is sizable, moving from 14 to almost 37 Å in elongation (Figure 1a). The corresponding volumes of the two conformers are shown in Figure 1b, leading to a cavitand expansion factor $J_{V\text{-}K} = V_{\text{Kite}}/V_{\text{Vase}} = 2.62$. The length of the wings determines the cavitand expansion factor. The most relevant parameters influencing the final NPR are the cavitand expansion ratio, the cavitand volume fraction, combined with the intrinsic rigidity of the PIM matrix. The average mechanical properties of the proposed auxetic polymer are estimated by knowing the cavitand volume expansion ratio $J_{V\text{-}K}$, the fraction $\Phi$ of the cavitand crosslinker in the polymer, and the mechanical characteristics of the polymer backbone. The micromechanical model of the auxetic polymer is detailed in the S.I. The experimentally measured Poisson's ratio of the standard **PIM1** is $\nu_0 \cong 0.38$, obtained experimentally using digital image correlation technique (DIC, Figure S13, Supporting Information).[36,37] According to our theoretical model, upon opening of the cavitand molecules the Poisson's ratio value starts from the nominal value $\nu_0 \cong 0.38$ and, by increasing the applied stretch, it rapidly decreases by reaching negative values (auxetic behavior, Figure 1c). The current Poisson's ratio, whose value depends on the applied stretch value $\lambda_x$, can be evaluated as follows:

$$\nu\left(\lambda_x\right) = -\frac{\lambda_{yt}-1}{\lambda_x-1} = -\frac{\lambda_{zt}-1}{\lambda_x-1} \tag{1}$$

Based on the randomness of the cavitand arrangement within the polymer network, which does not introduce any preferential direction in the material at the molecular scale, in Equation (1) it has been assumed that the Poisson's ratio is the same in the $x$-$y$ and $x$-$z$ planes, i.e., the material displays an isotropic 3D mechanical behavior.

The above-used total stretches $\lambda_{yt}$, $\lambda_{zt}$, taking place perpendicularly to applied stretch direction $x$, depend on both the applied deformation and on the cavitand switching from the vase to the kite conformation. The evaluation of the total stretches is detailed in the micromechanical theoretical model section of S.I. When all cavitands are open (cavitand opening factor $h = 1$, Figure 1c, bottom) the cavitand opening mechanism does not provide any further microscopic expansion to the material; by further increasing the applied stretch, the Poisson's ratio tends to reach that of the standard polymer without cavitand molecules. This happens because, for sufficiently high stretch values, the polymer network deformation is not affected anymore by the already completed cavitand expansion. As can be observed in Figure 1c, the earlier

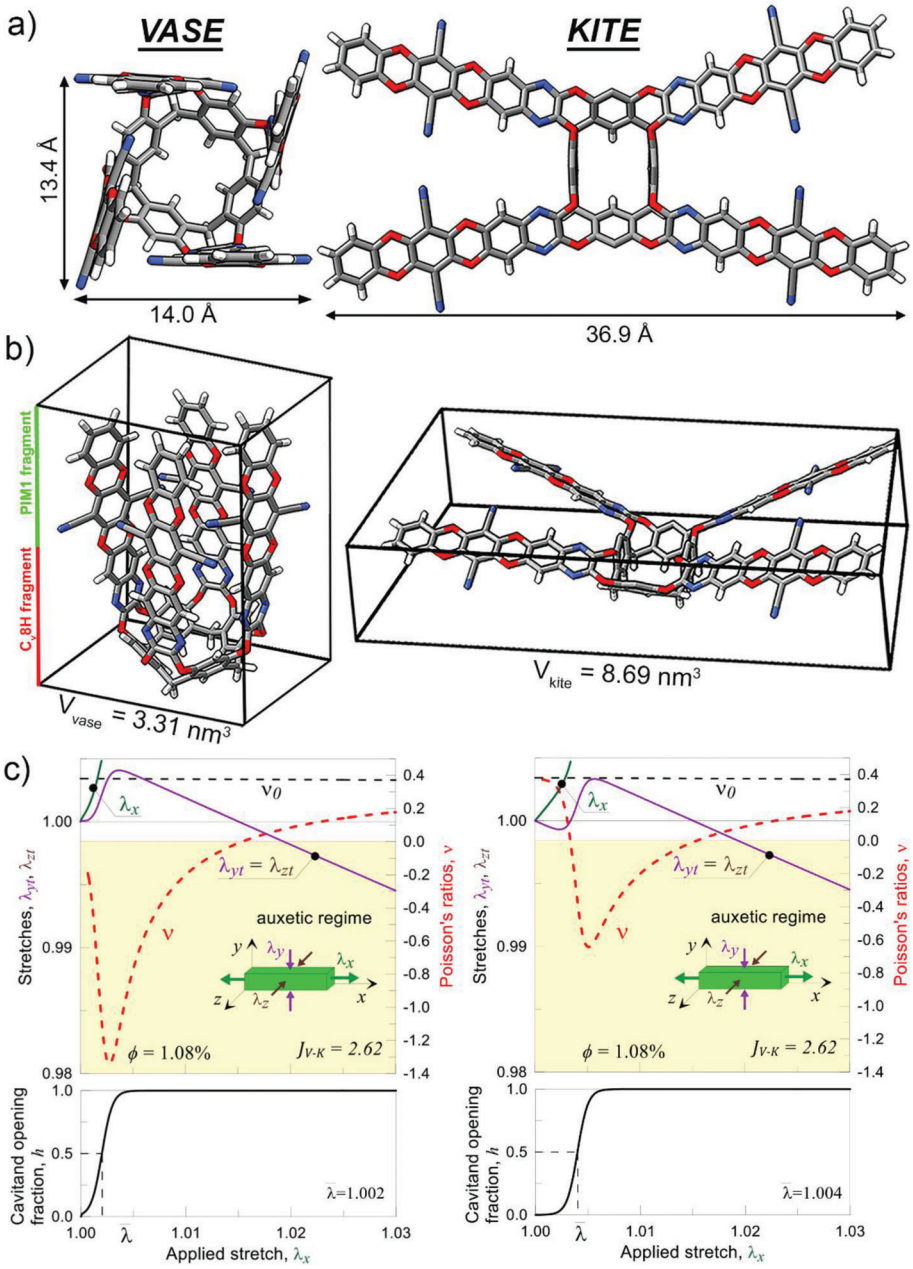


**Figure 1.** Theoretical prediction of the auxetic behavior: a) Spartan optimized structures of the auxeton in the vase and kite form with the respective dimensions; b) volume of the auxeton in the vase and kite forms; c) Poisson's ratio for a PIM with cavitand molecules (Φ = 1.08% vol) versus applied stretch $\lambda_x$. Transversal stretches $\lambda_y = \lambda_z$ are also represented. Different values of the parameter $\bar{\lambda}$ of the cavitand opening function *h* have been used to underline the effect of such a parameter characterizing the theoretical model on the calculated Poisson's ratio.

the cavitand begins to open (small values of the model parameter $\bar{\lambda}$ that defines the stretch at which half of the cavitands are open) the more auxetic is the material (Section 10.1, Supporting Information).

### 2.2. Experimental Implementation of the Theoretical Model

The envisioned molecular auxetic polymer is formed by two components: the rigid PIM and the cavitand acting as a cross-linking agent (Figure 2a). To avoid the conformational expansion that occurs in cavitands switching will be "absorbed" by the flexibility of the conformational changes of the polymer, the rigid **PIM1** derived from 5,5′,6,6′-tetrahydroxy-3,3,3′,3′-tetramethyl-1,1′-spirobiindane (**TTSBI**) and 2,3,5,6-tetrafluoroterephthalonitrile (**TFTPN**)[32] was selected as matrix. To effectively transduce the mechanical stimulation in the expansion of the auxetons, these dimensionally variable units have been inserted as a crosslinker in **PIM1** by covalently anchoring the four quinoxaline walls to the polymer backbone. To this purpose, a proper quinoxaline

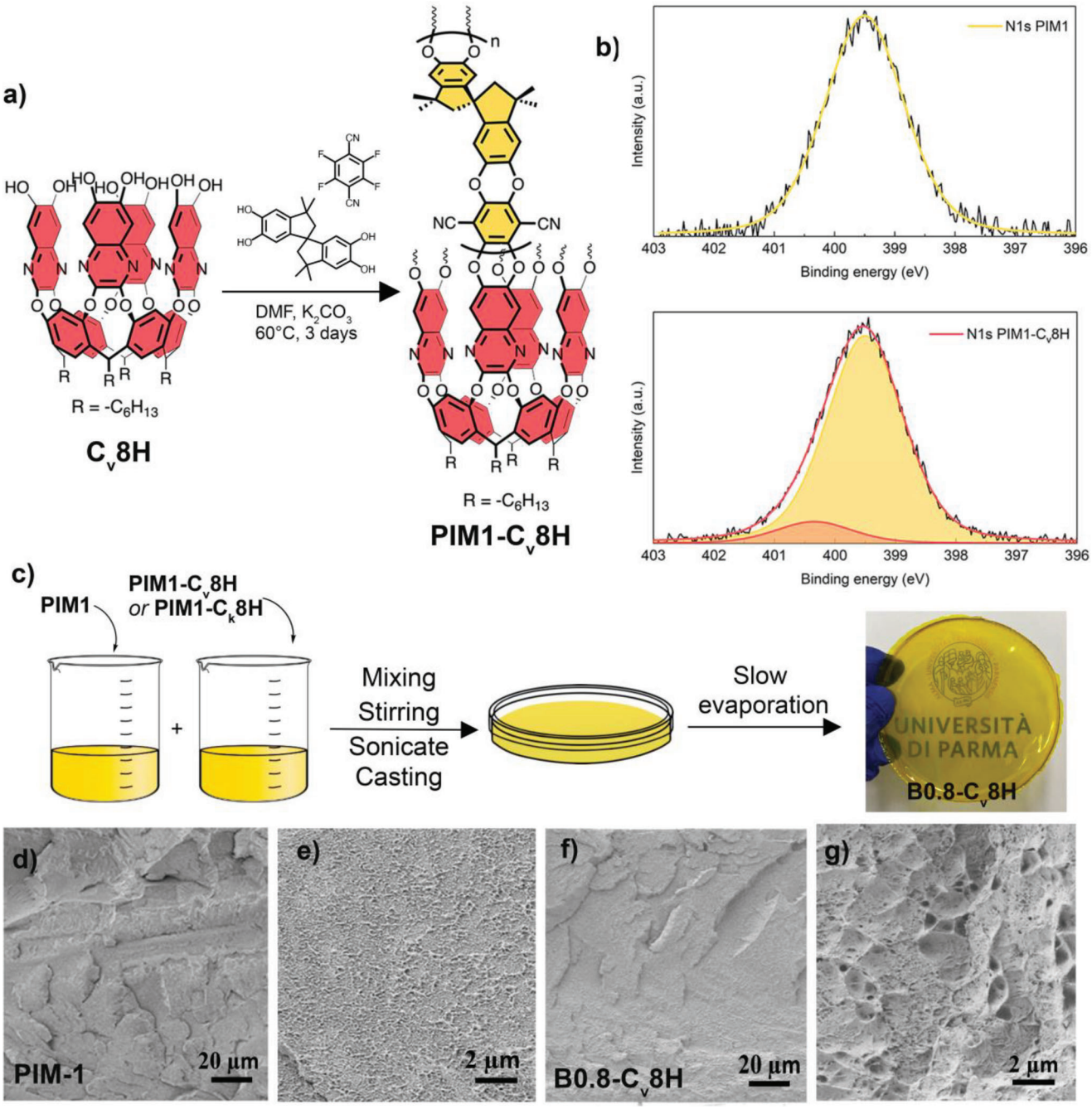


**Figure 2.** a) synthesis of **PIM1-$C_V$8H** (only one of the four polymer connections is shown for clarity); b) N1 core levels XPS analysis of **PIM1** and **PIM1-$C_V$8H**, showing the two different photoemission peaks related to the quinoxaline (orange) and nitrile (yellow) nitrogen atoms; c) scheme of the blends preparations and picture of **B0.8- $C_V$8H**; d,e) SEM images of fractured **PIM1** at different magnifications; f,g) SEM images of fractured **B0.8-$C_V$8H** at different magnifications.

cavitand bearing eight hydroxyl groups at the upper rim (**$C_V$8H**) was synthetized in two steps starting from the corresponding hexyl-footed resorcinarene **Res[$C_6H_{13}$, H]**. The scaffold was initially bridged with 2,3-dichloro-6,7-dimethoxyquinoxaline (Scheme S1, Supporting Information) to form a quinoxaline cavitand with eight methoxy groups at the upper rim. Excision of the methyl groups gave the desired cross-linker **$C_V$8H** (Scheme S2, Supporting Information, Figure 2a). The molecule was fully characterized by $^1$H and $^{13}$C NMR spectrometry and MS analysis (Figures S1–S3, Supporting Information). The triplet of the methine protons of the resorcinarene scaffold at 5.70 ppm in $^1$H NMR spectrum is diagnostic of the vase conformation of the cavitand in solution.[25] The corresponding fixed kite **$C_K$8H** cavitand, used as the control crosslinker, was prepared following

the same synthetic procedure using **Res[$C_6H_{13}$, $CH_3$]** as starting material (Scheme S3, Figures S4–S6, Supporting Information). The introduction of four methyl groups in the apical position of the resorcinarene forces the corresponding cavitand to assume a blocked kite conformation, as confirmed by the shift of the methine signal at 3.60 ppm in $^1$H NMR spectrum.[35,38]

The synthesis of the crosslinked network **PIM1-$C_V$8H** was conducted by adapting the standard **PIM1** recipe (Figure 2a).[39] Considering that **$C_V$8H** has twice as many functional groups of **TTSBI**, the starting molar ratio of **TTSBI**/**$C_V$8H** was set to 0.92/0.04, corresponding to ≈12% w/w of auxeton in the final **PIM1-$C_V$8H**.

The detailed synthetic procedure is reported in the S.I. The same procedure was employed to prepare **PIM1-$C_K$8H**, by replacing the vase cavitand **$C_V$8H** with its fixed kite analogue **$C_K$8H** (Scheme S4, Supporting Information). The effective embedding of **$C_V$8H** into the **PIM1** matrix was confirmed by IR spectroscopy, comparing the spectra of **PIM1-$C_V$8H**, **PIM1**, and **$C_V$8H** (Figure S7, Supporting Information). Indeed, typical nitrile stretching at 2240 cm$^{-1}$ of **PIM1** and the –C≐N—C– peak at 1572 cm$^{-1}$, referred to as the quinoxaline walls, are both present in the final polymer.

The presence and the amount of cavitand in the crosslinked polymer was evaluated via X-ray photoelectron spectroscopy (XPS) analyses (Figure 2b) from the study of the N1s core levels. Contrary to **PIM1**, which possesses only the nitrogen species relative to the nitrile –C≡N, **PIM1-$C_V$8H** shows an additional photoemission referred to the quinoxaline ring nitrogen –C≐N–. Figure 2b (top) shows the N1s core level for **PIM1**; the main peak at ≈399.50 eV (full width at half-maximum FWHM = 1.5 eV) is related to nitrile groups.[40] The N1s core level analysis of **PIM1-$C_V$8H** and **PIM1-$C_K$8H** are shown in Figure 2b (bottom) and Figure S8, Supporting Information, respectively: the main component, related to nitrile groups observed in **PIM1**, is still located at 399.50 eV (FWHM 1.5 eV), while a second weak component is present at ≈400.25 eV (FWHM 1.5 eV). The latter is related to the quinoxaline C≐N–C species in **PIM1-$C_{V/K}$8H**, as already observed in quinoxaline-based molecules[41,42] and cavitand-bearing polythiophenes.[43] This second peak is the evidence of the cavitand presence in the polymer, while the intensity ratio between the two components determines the amount of **$C_{V/K}$8H** crosslinker effectively incorporated into **PIM1-$C_{V/K}$8H**.

For **PIM1-$C_K$8H** this value mirrors the molar ratio of the monomers in the reaction medium, while the percentage of **$C_V$8H** inserted in the **PIM1-$C_V$8H** polymer is estimated in 8.0% w/w, as detailed in the Supporting Information. We can speculate that the lower reactivity of **$C_V$8H** compared to **$C_K$8H** is due to steric reasons, i.e., to the closed proximity of the OH groups in the reacting cavitand. Traces of fluorine (<1%) were detected in all samples, related to the presence of a small amount of **DFTPN** as a terminal unit.

The thermal stability of **PIM1-$C_V$8H** was determined via thermogravimetric analysis (TGA, Figure S9, Supporting Information). A small weight loss, ascribable to the presence of residual solvent trapped in the pores, was observed at temperature below 200 °C, followed by thermal degradation ≈400 °C, which is in line with the TGA profile of pristine **PIM1** (Figure S9, Supporting Information).

**PIM1** films were prepared by solvent casting from chloroform solutions. A film of pristine **PIM1** ($M_w$ = 79 KDa; PDI = 1.50) was prepared for a blank experiment dissolving 1.3 g of **PIM1** in 25 mL of chloroform. The solvent was allowed to slowly evaporate at room temperature over 48 h. Crosslinked **PIM1-$C_V$8H** and **PIM1-$C_K$8H** are insoluble in solvents commonly used for **PIM1**, jeopardizing the formation of the corresponding films via solvent casting. To overcome this problem, a blending strategy[44] was selected for the preparation of crosslinked films, consisting of mixing a dispersion of **PIM1-$C_V$8H** in chloroform with a solution of **PIM1** in the same solvent (Figure 2c). Four different blends were prepared to investigate the effect of the quantity of cavitands present in the network on its auxeticity, named **B0.1-$C_V$8H**, **B0.4-$C_V$8H**, **B0.8-$C_V$8H**, **B1.2-$C_V$8H**. The number after the letter B (blend) is referred to 0.1, 0.4, 0.8, 1.2% w/w of **PIM1-$C_V$8H** portion in the final film. The quantity of each component used for the blends are reported in Table S2, Supporting Information. **B1.2-$C_K$8H** was prepared accordingly. Defects start to appear in the films upon increasing the amount of crosslinked polymer in the blend, resulting in opacity for the more concentrated **B1.2-$C_V$8H** (Figure S10, Supporting Information). On the contrary, **B1.2-$C_K$8H** remained transparent (Figure S10, Supporting Information). Therefore, **B1.2-$C_V$8H** will not be discussed from now onward.

The blend morphology was investigated by scanning electron microscopy (SEM). The cross sections were obtained by freeze fracturing the specimens (**PIM1**, **B0.4-$C_V$8H**, **B0.8-$C_V$8H**, **B1.2-$C_K$8H)** in liquid nitrogen and the relative images are provided in Figure S11. None of the samples shows macro- or mesoscopic defects along the cross-section, indicating the formation of a dense material. As highlighted in Figure 2d-g, at higher magnification **PIM1** presents a jagged pattern, while blends have a more rough/corrugated structure, with alveoli surrounded by the same **PIM1** microstructure.

### 2.3. Experimental Evidence of Auxeticity and Quantitative Prediction of the Observed Auxeticity

The predicted vase-to-kite conformational switch responsible for the NPR in the material, triggered by tensile elongation, is sketched in **Figure 3**a. Mechanical tests were performed by stretching the polymer specimens, prepared in the shape of thin strips (size 10 × 50 × 0.2 mm). Tensile tests until the final failure as well as tensile cyclic tests were performed on at least three specimens of the same blend. The elastic modulus of the blends is comparable to that of pristine **PIM1**. **PIM1** shows a greater decrease of the tangent Young's modulus with the deformation (Figure S12, Supporting Information, top), while the blend tends to have a more linear elastic behavior (slight decrease of the tangent Young's modulus with the applied deformation, Figure S12, Supporting Information, bottom) and results to be more brittle, showing a lower maximum deformation at failure. The deformation was applied at a small rate equal to $\lambda_x = 5 \times 10^{-4}\ s^{-1}$. Pictures of the sample at equally spaced time instants were taken with a high-resolution camera, and then used in DIC to obtain the strains of the material in the stretched and transversal direction (Figure 3b).

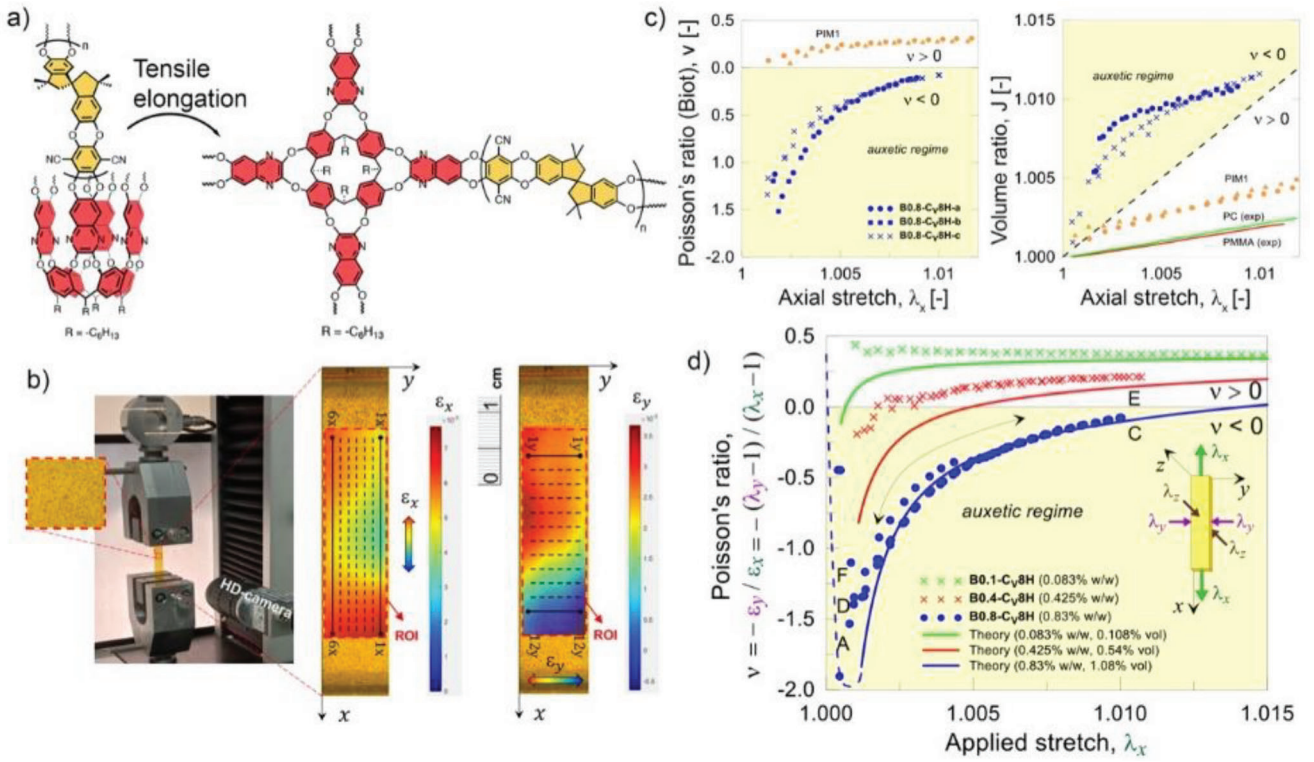


**Figure 3.** a) Molecular representation of vase to kite conformational switch triggered by tensile elongation; b) Mechanical Test setup with the high-resolution camera for the DIC elaboration (left). DIC images of the specimen showing the longitudinal and transversal strain maps determined in the Region Of Interest (ROI, right); virtual strain gauges are sketched as dashed lines; c) Trend of the NPR and of the volume ratio versus the applied stretch for **PIM1** and **B0.8-C$_V$8H** specimen. d) Comparison of the average Poisson's ratio versus the applied stretch $\lambda_x$ obtained from experimental tests and that provided by the theoretical model for different cavitand molecule contents (0.1% w/w; 0.4% w/w; 0.8% w/w). The corresponding volume fractions of the cavitand molecules are also indicated. The specimens **B0.1-C$_V$8H** and **B0.4-C$_V$8H** were tested under simple uniaxial tension, while the specimen **B0.8-C$_V$8H** was tested under two identical uniaxial stretch cycles (letters A-C-D-E-F, see Figure 5b).

The prediction of the Poisson's ratio through the theoretical micromechanical model is performed firstly by determining the parameters $\bar{\lambda}$, $c$; they are used in Equation (8) of the Supporting Information. for calculating the fraction $h$ of cavitand molecules switched from the vase to the kite conformation at a given applied stretch level $\lambda_x$. In particular, the above-mentioned values were determined by best fitting the average experimentally determined Poisson's ratio versus stretch curve of the case **B0.8-C$_V$8H** and resulted to be: $\bar{\lambda} = 1.002$, $c = 0.005$. These values were adopted for estimating the Poisson's ratio as follows:

- The average stretches $\lambda_c$ of the cavitand molecules are evaluated by using Equation (12) of the S.I., where $J_{V\text{-}K} = 2.62$ (Figure 1b), ϕ is the volume fraction of the cavitand molecules in the polymer, and $h$ is determined as detailed in Equation (8) of the Supporting Information.;
- The stretches $\lambda_{yc} = \lambda_{zc}$ arising in the material due to cavitand molecules opening are determined by using Equation (11) of the S.I.;
- The total stretch $\lambda_{yt}$ (i.e., due to mechanical deformation and to the cavitand opening) in direction $\gamma$ is determined through Equation (13) of the S.I.;
- The Poisson's ratio $\nu(\lambda_x)$ is finally determined by using Equation (1).

The DIC experimental NPR trend of the best-performing blend **B0.8-C$_V$8H** is reported in Figure 3c (left) for three different film specimens, while the corresponding volume ratio is shown in Figure 3c (right). The volume ratio of **PIM1**, polycarbonate (PC), and polymethylmethacrylate (PMMA) are outlined for comparison.[45]

In Figure 3d the average Poisson's ratio values determined from DIC measurements are illustrated for three different cases, namely **B0.1-C$_V$8H** (0.1% w/w), **B0.4-C$_V$8H** (0.4% w/w), and **B0.8-C$_V$8H** (0.8% w/w). Blend **B1.2-C$_V$8H** is excluded because its inhomogeneity led to irreproducible NPR values (Figure S14, Supporting Information). For the first two cases, a simple tensile test has been performed, while two identical tensile cycles (each one up to the maximum deformation $\epsilon_x = 1\%$) have been applied to the specimen made of **B0.8-C$_V$8H**. The case with 0.1% crosslinking auxeton does not show any auxeticity, while for the polymer **B0.4-C$_V$8H** NPR emerges for small deformation values and quickly disappears as the applied stretch increases. Finally, the case **B0.8-C$_V$8H** shows a quite large NPR (up to ≈−2) for low values of the applied deformation; proceeding further with stretching the material, the Poisson's ratio increases and tends

to the value typical of the **PIM1** polymer. The maximum auxeticity appears for low values of the applied deformation due to transversal deformation caused by the cavitands opening, which is larger in comparison to the axial stretch. As far as the longitudinal stretch increases, the cavitands molecules are almost all open and their expansion effects is not effective anymore in inducing the auxetic response. The application of two identical tensile cycles of Figure 3d for the case **B0.8-$C_V$8H** has been performed to prove the reproducibility of the NPR response. It is worth mentioning that for very low values of the applied deformation ($1 \leq \lambda_x < \approx 1.001$), the determination of the Poisson's ratio is not reliable due to the excessively small values of the displacements, which cannot be precisely managed by the DIC measurements. The theoretical fitting performed through the model illustrated above are reported in Figure 3d with continuous lines; both the trend and the determined values are in satisfactory agreement with the experimental outcomes. The theory provides the same increasing trend of the Poisson's ratio with increasing the applied axial deformation; in the case of **B0.8-$C_V$8H**, the Poisson's ratio negativity ends when the applied deformation is roughly equal to $\lambda_x \approx 1.015$.

Due to the thin conformation of the specimen lying on the *x*-*y* plane, the deformation on the *y*-*z* plane cannot be determined from the DIC measurements. These polymers are processable only via solvent or freeze casting leading to films of limited thickness (<1 mm),[46] not compatible with DIC analysis, which requires a thickness of at least 3–4 mm. Being the tested films completely amorphous and isotropic (Figure S15, Supporting Information), the measured transversal deformation $\lambda_y$ is expected to be the same as that taking place along the other transversal direction *z*, namely $\lambda_z$. Albeit presently not experimentally measurable, the emerging auxetic behavior is potentially tridimensional, leading to a 3D molecular auxetic.

### 2.4. Control Experiments

Two control experiments have been devised and conducted to prove that the auxetic behavior of **PIM1-$C_V$8H** is solely due to the mechanically driven conformational expansion of the cavitand crosslinker. The first control experiment was implemented to prove that covalent crosslinking of the auxeton through the quinoxaline wings is necessary to induce the conformational switch. To this purpose, vase and kite cavitands lacking of hydroxyl groups at the upper rim ($C_V$ and $C_K$, respectively) were homogenously dispersed in **PIM1** in a 1% w/w ratio to give **PIM1-$C_V$** and **PIM1-$C_K$** respectively (Figure S17, Supporting Information). The corresponding specimens were prepared and tested. In both cases, no auxetic behavior was observed, with measured Poisson's ratio values close to the value $\nu_0$ of pristine **PIM1** and a volume ratio trend typical of a non-auxetic material (**Figure 4**a).

A second, more demanding control experiment was devised to prove that the cavitand molecular expansion is the origin of auxeticity. This test required the synthesis of **PIM1-$C_K$8H** and its blending with **PIM1** in a 10% w/w ratio, to give **B1.2-$C_K$8H** (Figure S10, Supporting Information), to compare with **B0.8-$C_V$8H**, the best performing auxetic blend. The introduction of four methyl groups in the apical position of the resorcinarene scaffold forces the corresponding cavitand to assume the blocked kite conformation,[35] rendering **B1.2-$C_K$8H** the perfect candidate for the test. The results of the DIC analyses on three stretched specimens are reported in Figure 4b. None of them showed auxetic behavior, validating the cavitand conformational switching as the unique source of the material auxeticity.

### 2.5. Reversibility of the Auxetic Behavior

In order to verify the reversibility of the auxetic response induced by the crosslinking auxeton, cyclic tensile tests were performed. In particular, **B0.8-$C_V$8H** was tested by applying two subsequent cycles in which the specimen has been deformed with a constant stretch rate up to about a longitudinal deformation equal to $\lambda_x = 1.01$ (A-C), then unstretched to zero (C-D), followed by an identical second deformation cycle (D-E-F, Figure 5b).

The behavior of **B0.8-$C_V$8H** is compared to that of **PIM1**, for which one single deformation cycle was applied (**Figure 5**a). The strains in the longitudinal ($\epsilon_x$) and transversal ($\epsilon_y$) directions were determined from DIC measurements; the average value and the standard deviation of the strains were determined by using several measurements done within the ROI area (Figure 3b).

The transversal deformation of the **PIM1** specimen results to be negative (pink curve Figure 5a), indicating a contraction of the material, while for the **B0.8-$C_V$8H** specimen the transversal deformation results to be positive (pink curve Figure 5b), corresponding to an expansion of the material transversally to the tensile direction (auxetic behavior). It is worth noting that for the **B0.8-$C_V$8H** specimen the transversal deformation increases (part A-B' in Figure 5b) by stretching the material up to a certain value, then it slightly decreases (part B'-C' in Figure 5b) even if the material is further stretched (B-C). This is due to the early opening of the cavitand molecules, which occurs for low stretching values. As soon as all the cavitand molecules are open, the macroscopically detectable expansion is not promoted anymore by the auxeton and the material starts behaving as a standard **PIM1** specimen, so the transversal deformation decreases. Upon unstretching (C-D), the longitudinal deformation decreases and the transversal one increases a little and then goes back to zero (point D in Figure 5b). During the second cycle (D-E-F), the same trend was observed, confirming that the conformational opening/closing mechanism of the cavitand molecules is fully reversible. This behavior is confirmed also by observing the Poisson's ratio versus stretch curve reported in Figure 3d: upon stretching and unstretching the trend of the curve $\nu(\lambda_x)$ is almost superimposable during the two subsequent cycles. A more extensive stretch cycling test has been conducted on a **B0.8-$C_V$8H** specimen to test more thoroughly the reproducibility of NPR behavior upon repeated loading cycles. The results, shown in Figure S20, Supporting Information, for five runs, confirm the complete reversibility of the auxetic behavior.

## 3. Conclusions

The long-standing problem of generating artificial molecular auxetics has now a promising solution. The proposed auxetic polymer does not mimic metamaterials at the molecular level like rotating triangles,[11] egg rack structures,[12] or reentrant honeycombs.[13] Instead, it relies on a completely novel approach

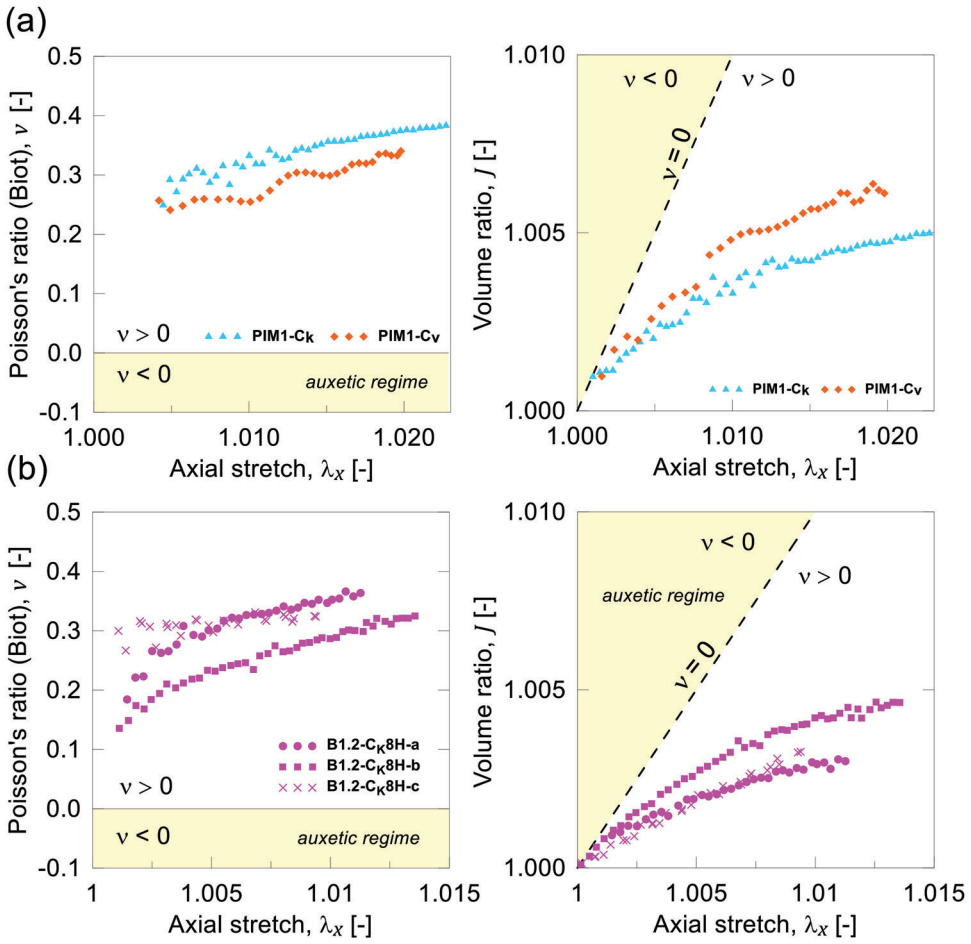


**Figure 4.** **PIM1** specimens with dispersed cavitand molecules both in the vase (**PIM1-C$_V$** red dots) and in the kite (**PIM1-C$_K$** blue dots) conformations. Poisson's ratio (left) and average volume ratio (right) versus the applied stretch $\lambda_x$ determined from DIC analyses; b) **B1.2-C$_K$8H** specimens with crosslinked cavitand molecules in the kite conformations. Poisson's ratio (left) and volume ratio (right) versus the applied stretch $\lambda_x$ determined from DIC analyses for three tested specimens.

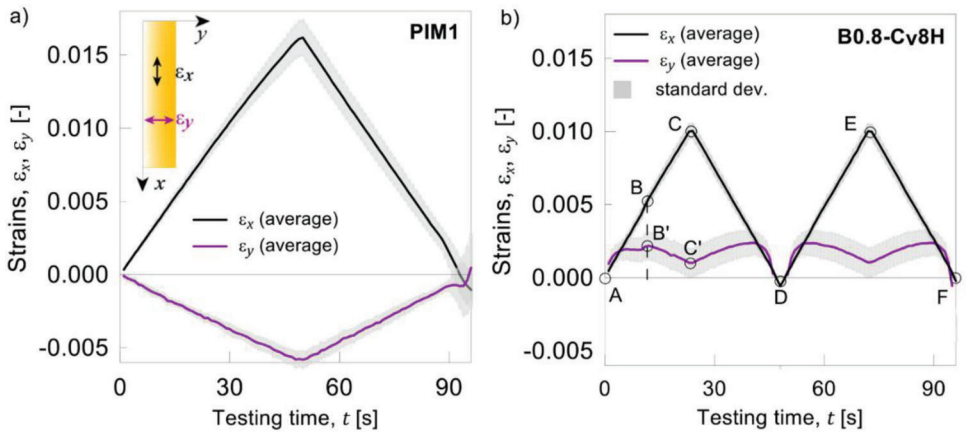


**Figure 5.** Average strain $\epsilon_y = \lambda_y - 1$ determined from experimental tests versus the applied stretch $\epsilon_x = \lambda_x - 1$. a) Standard **PIM1** subjected to one stretch cycle; b) **B0.8-C$_V$8H** subjected to two stretch cycles. It can be noted that under an applied tensile (positive) deformation $\epsilon_x$ the transversal deformation $\epsilon_y$ is negative (contraction) for **PIM1**, while it is positive (expansion) for **B0.8-C$_V$8H**. The reversibility of the deformation is clearly visible, being the two deformation cycles almost identical. The standard deviation shown in the figure is evaluated by using the measurements provided by the virtual extensometers of the DIC analysis (6 in *x*-direction and 12 in *y*-direction, see Figure 3b) placed on a single specimen.

of mechanically-driven conformational expansion of a cavitand, which has the unique property to switch between two well-defined conformations: the compact vase and the extended kite. The macroscopic expression of cavitands conformational expansion is obtained by introducing the cavitand auxetic unit as crosslinkers in a PIM. In this way, the two discrete conformational states of the cavitand provide the desired kinematic response responsible of the NPR at the macroscopic level.

The **PIM1** polymer matrix presents a rigid structure capable to transfer the mechanical stress into a conformational expansion of the crosslinking unit. The conformational expansion propagates to the polymer backbone, triggering the NPR in the material. On the cavitand side, the direct covalent linking of the quinoxaline wings to the PIM structure combined with its conformational flexibility are the requirements to be mechanically responsive, as proven by the two control experiments. At present, the NPR has been experimentally measured in the *x*-*y* plane only and not in the *x*-*z* plane, since the blends are processable only via solvent casting, leading to films of no more than 200–220 µm thickness (Figure S11, Supporting Information). The DIC technique requires a thickness of at least 3–4 mm for reliable NPR evaluation. Nevertheless, being the films' microstructure completely amorphous and isotropic, the material can be reasonably assumed to be isotropic also from the mechanical viewpoint. Therefore, **PIM1-$C_V$8H** is expected to behave as a 3D molecular auxetic, according to the prediction provided by the developed theoretical model.

The auxeton micromechanical model proposed is able to match both the observed experimental NPR values and the kinematic behavior of the material, validating the cavitand conformational expansion as the origin of the auxeticity. The agreement of the theory with the experimental data bodes well for the use of this model to design other auxetic materials and predict their NPR values.

Finally, the complete reversibility of the auxetic response singles out this material as a promising candidate for the fabrication of auxetic objects. Work is in progress to obtain the solution-processable version of this auxetic PIM, overcoming the processability limits of the present material.

## 4. Experimental Section

*General Polymerization Procedure*: **TTSBI** (0.92 eq.) and **$C_V$8H/$C_K$8H** (0.04 eq.) were dissolved in dry DMF (40 mL). Anhydrous potassium carbonate (4.5 eq.) was added to the solution and the mixture was kept stirring at room temperature for 15 min, then the addition of **TFTPN** (1 eq.) was followed. The reaction was carried out at 60 °C for 3 days, observing the formation of a yellow precipitate. The mixture was quenched in water, allowing the precipitation of the polymer that was filtered and washed several times with water and methanol. The product was further purified by refluxing in water for 4 h. The product was recovered as a yellow powder after filtration and dried in a vacuum oven at 60 °C for 2 days.

*General Procedure for Blend Preparation*: **PIM1** was dissolved in chloroform and stirred overnight at room temperature. In parallel, a dispersion of **PIM1-$C_V$8H**/**PIM1-$C_K$8H** in chloroform was prepared and stirred overnight at room temperature. The two samples were mixed, highly stirred for 3 h, and then sonicated using an ultrasonic homogenizer (Hielscher UP200Ht, 200 W, 26 KHz) for 20 min. The dispersion was casted in a Petri dish (9 cm ∅), kept in a closed environment under a gentle flow of nitrogen that allowed the slow evaporation of the solvent over 48–72 h.

*NMR Spectroscopy*: NMR spectra were collected on Bruker Avance 400 (400 MHz) and JEOL ECZ600R (600 MHz) spectrometer at 25 °C. $^1$H and $^{13}$C NMR chemical shifts ($\delta$) are given in part per million (ppm) and calibrated to either residual solvent signal.

*Mass Spectrometry*: High-resolution ESI-MS was performed using an LTQ ORBITRAP XL Thermo spectrometer. High-resolution MALDI-TOF was performed using an AB SCIEX MALDI TOF-TOF 4800 Plus (matrix: $\alpha$-cyano-4-hydroxycinnamic acid). GC-MS analyses were performed using an Agilent Technologies 6890N Network GC System.

*Computational Modeling*: Modeling studies were carried out by means of molecular mechanics (MM) calculations, using the Spartan 16 MMFF force field.[47]

*X-Ray Photoelectron Spectroscopy (XPS)*: XPS analyses were performed in an Ultra-High-Vacuum (UHV) system using a VSW HA100 hemispherical electron energy analyzer with PSP power supply and control and a non-monochromatized Mg K$\alpha$ source (photon at 1253.6 eV), with a final energy resolution of 0.86 eV.[48] The binding energy (BE) scale were calibrated from the Au4f 7/2 peak at 84.0 eV of a sputtered Au surface. The core level analysis was performed by Voigt line-shape deconvolution after the background subtraction using a Shirley function. The typical precision for each component's energy position is ±0.05 eV. The uncertainty for the full width at half-maximum (FWHM) is less than ± 2.5%, while it is about ± 2% for the area evaluation.

*ATR-IR Spectroscopy*: Infrared absorption spectroscopy analyses were performed with a Perkin Elmer FT-IR Spectrum Two instrument using powder samples. The background was subtracted from every spectrum recorded.

*TGA Analysis*: TGA analysis were performed on a Perkin Elmer TGA 8000. Heating run: 25° to 900 °C at 10 °C min$^{-1}$, in air.

*Scanning Electron Microscopy (SEM)*: The morphology and composition of the samples were investigated with a Zeiss Auriga Compact Field-Emission SEM. SEM images were acquired by using 1 kV acceleration voltages of the primary electron beam.

*Tensile Tests*: Mechanical testing has been performed by using a universal testing machine Galdabini Quasar 2.5 on rectangular specimens having the size 50 × 10 × 0.2 mm. A tensile stretch was applied to the specimens at a constant deformation rate equal to $\lambda_x = 5 \times 10^{-4}$ s$^{-1}$ until the maximum deformation was reached. The specimens have been prepared for mechanical testing by spray-painting a pattern of small irregular dots (size roughly between 0.1 and 0.5 mm) whose position is tracked and the displacements quantified by the subsequent DIC analyses. Single or double-cycle tensile mechanical tests have been conducted by recording the force and displacement with a frequency of 10 Hz, while pictures of the specimen (to be used in the digital image correlation (DIC) analyses) have been acquired by a Basler acA5472-17uc USB 3.0 camera with a resolution of ≈3000 × 1000 pixels at a frequency of 1 Hz.

*DIC Measurements*: The DIC analyses have been conducted by using the Ncorr[49] software by setting the region of interest (ROI, with a size equal to ≈30 × 7 mm). The deformations along the *x*- and the *y*-directions have been determined through the Ncorr post processing software. The average deformations required to determine the Poisson's ratio have been obtained by considering the values of the deformations evaluated through 6 virtual extensometers placed in *x*-direction for determining the average deformation $\lambda_x$ and 12 virtual extensometers placed in *y*-direction for determining the average deformation $\lambda_y$.

*Statistical Analysis*: The experimental data were not preprocessed additionally and presented as mean ± standard deviation (SD). The measurements obtained from the mechanical tests have been processed as described below. Firstly, the size of each specimen's cross-section was obtained from a set of three different measures, taken by using a caliber with 0.01 mm precision, at three different locations along the specimen length. The average size values of the cross-section were used to evaluate the cross-section area adopted to determine the nominal stress value in the specimen. The load applied to the specimen was recorded by a load cell with a precision of 0.0125 N while the longitudinal displacements were recorded with a transducer having precision equal to 0.081 mm.

For each kind of blend, at least six specimens were prepared and tested under the same stretch rate. After performing the DIC analysis for every

single specimen, several virtual extensometers have been place in the ROI: 6 in $x$-direction and 12 in $y$-direction, see Figure 3b). The average stretch values in the $x$- and $y$-direction have been determined by averaging the values provided by the above-mentioned multiple virtual extensometers; finally, the Poisson's ratio has been obtained by using Equation (1), while the volume ratio has been obtained by using Equation (10 S.I.). The mechanical properties shown in Figure S12, Supporting Information, represent the average value (the SD is also displayed as a grey region) obtained by considering all the tested specimens made of the same material. The tangent Young's modulus, $E' = \Delta\sigma/\Delta\lambda_x$, has been numerically obtained by determining the slope of the $\sigma-\lambda_x$ curve by adopting a smoothing stretch distance equal to $\Delta\lambda_x = 0.0005$. The corresponding SD has also been determined relying on the same obtained values.

## Supporting Information

Supporting Information is available from the Wiley Online Library or from the author.

## Acknowledgements

This work benefited from the equipment and framework of the COMP-HUB Initiative, funded by the Departments of Excellence program of the Italian Ministry for Education, University, and Research (MIUR, 2023–2027). R. P. thanks the University of Parma intramural funding "Bando di Ateneo per la Ricerca 2021". Centro Interfacoltà di Misure "G. Casnati" of the University of Parma is acknowledged for the use of NMR and MS facilities. The authors thank Dr. G. Trevisi of IMEM-CNR for SEM images, Dr. L. Aversa of IMEM-CNR for XPS analyses, Mr. D. Marchetti for Spartan calculations, and Prof. A. Pucci of the University of Pisa for the GPC analysis of PIM1.

## Conflict of Interest

The authors declare no conflict of interest.

## Data Availability Statement

The data that support the findings of this study are available from the corresponding author upon reasonable request.

## Keywords

Cavitands, conformational switch, molecular auxetic, polymers of intrinsic microporosity

Received: July 6, 2023
Revised: August 23, 2023
Published online:

[1] K. E. Evans, M. A. Nkansah, I. J. Hutchinson, S. C. Rogers, *Nature* **1991**, *353*, 124.
[2] K. E. Evans, A. Alderson, *Adv. Mater.* **2000**, *12*, 617.
[3] G. N. Greaves, A. L. Greer, R. S. Lakes, T. Rouxe, *Nat. Mater.* **2011**, *10*, 823.
[4] R. Lakes, *Science* **1987**, *235*, 1038.
[5] R. Gatt, L. Mizzi, J. I. Azzopardi, K. M. Azzopardi, D. Attard, A. Casha, J. Briffa, J. N. Grima, *Sci. Rep.* **2015**, *5*, 8395.
[6] A. A. Pozniak, K. W. Wojciechowski, J. N. Grima, L. Mizzi, *Composites, Part B* **2016**, *94*, 379.
[7] Z. Zheng, J. Li, K. Wei, N. Tang, M.-H. Li, J. Hu, *Adv. Mater.* **2023**, *35*, https://doi.org/10.1002/adma.202304631.
[8] K. W. Wojciechowski, *Mol. Phys.* **1987**, *61*, 1247.
[9] K. W. Wojciechowski, A. C. Brańka, *Phys. Rev. A* **1989**, *40*, 7222.
[10] R. H. Baughman, D. S. Galvão, *Nature* **1993**, *365*, 735.
[11] J. N. Grima, K. E. Evans, *Chem. Commun.* **2000**, 1531.
[12] J. N. Grima, J. J. Williams, K. E. Evans, *Chem. Commun.* **2005**, 4065.
[13] N. Pour, L. Itzhaki, B. Hoz, E. Altus, H. Basch, S. Hoz, *Angew. Chem. Int. Ed.* **2006**, *45*, 5981.
[14] C. He, P. Liu, A. C. Griffin, *Macromolecules* **1998**, *31*, 3145.
[15] C. He, P. Liu, P. J. McMullan, A. C. Griffin, *Phys. Stat. Sol.* **2005**, *242*, 576.
[16] Y. Suzuki, G. Cardone, D. Restrepo, P. D. Zavattieri, T. S. Baker, F. A. Tezcan, *Nature* **2016**, *533*, 369.
[17] D. Mistry, S. D. Connell, S. L. Mickthwaite, P. B. Morgan, J. H. Clamp, H. F. Gleeson, *Nat. Commun.* **2018**, *9*, 5095.
[18] A. C. Brańka, D. M. Heyes, K. W. Wojciechowski, *Phys. Status Solidi B* **2009**, *246*, 2063.
[19] T. Raistrick, Z. Zhang, D. Mistry, J. Mattsson, H. F. Gleeson, *Phys. Rev. Res.* **2021**, *3*, 023191.
[20] D. J. Cram, *Science* **1983**, *219*, 1177.
[21] D. J. Cram, J. M. Cram, *Container Molecules and Their Guests*, RSC, Cambridge **1994**.
[22] F. Tancini, E. Dalcanale, in *Supramolecular Polymer Chemistry* (Ed. A. Harada), Wiley-VCH Verlag Gmbh & Co. KGaA, Weinheim, Germany **2012**, pp. 71–126.
[23] M. Dionisio, L. Ricci, G. Pecchini, D. Masseroni, G. Ruggeri, L. Cristofolini, E. Rampazzo, E. Dalcanale, *Macromolecules* **2014**, *47*, 632.
[24] I. Pochorovski, F. Diederich, *Acc. Chem. Res.* **2014**, *47*, 2096.
[25] J. R. Moran, J. L. Ericson, E. Dalcanale, J. A. Bryant, J. C. B. Knobler, D. J. Cram, *J. Am. Chem. Soc.* **1991**, *113*, 5707.
[26] P. J. Skinner, A. G. Cheetham, A. Beeby, V. Gramlich, F. Diederich, *Helv. Chim. Acta* **2001**, *84*, 2146.
[27] P. Pagliusi, F. Lagugné-Labarthet, D. K. Shenoy, E. Dalcanale, Y. R. Shen, *J. Am. Chem. Soc.* **2006**, *128*, 12610.
[28] P. Amrhein, A. Shivanyuk, D. W. Johnson, J. Rebek, *J. Am. Chem. Soc.* **2002**, *124*, 10349.
[29] M. Frei, F. Marotti, F. Diederich, *Chem. Commun.* **2004**, *10*, 1362.
[30] I. Pochorovski, *Ph.D. thesis*, ETH Dissertation Nr. 21351, ETH Zürich, **2013**.
[31] M. Torelli, F. Terenziani, A. Pedrini, F. Guagnini, I. Domenichelli, C. Massera, E. Dalcanale, *ChemistryOpen* **2020**, *9*, 261.
[32] P. M. Budd, B. S. Ghanem, S. Makhseed, N. B. McKeown, K. J. Msayib, C. E. Tattershall, *Chem. Commun.* **2004**, 230.
[33] Z.-X. Low, P. M. Budd, N. B. McKeown, D. A. Patterson, *Chem. Rev.* **2018**, *118*, 5871.
[34] E. Dalcanale, P. Soncini, G. Bacchilega, F. Ugozzoli, *J. Chem. Soc., Chem. Commun.* **1989**, 500.
[35] K. L. Pirondini, A. G. Stendardo, S. Geremia, M. Campagnolo, P. Samorì, J. P. Rabe, R. Fokkens, E. Dalcanale, *Angew. Chem., Int. Ed.* **2003**, *42*, 1384.
[36] L. Francesconi, M. Taylor, K. Bertoldi, A. Baldi, *Exp. Mech.* **2018**, *58*, 283.
[37] T. Fíla, P. Koudelka, P. Zlámal, J. Falta, M. Adorna, M. Neuhäuserová, J. Luksch, O. Jiroušek, *Adv. Eng. Mater.* **2019**, *21*, 1900204.
[38] D. J. Cram, H.-J. Choi, J. A. Bryant, C. B. Knobler, *J. Am. Chem. Soc.* **1992**, *114*, 7748.
[39] P. M. Budd, E. S. Elabas, B. S. Ghanem, S. Makhseed, N. B. McKeown, K. J. Msayib, C. E. Tattershall, D. Wang, *Adv. Mater.* **2004**, *16*, 456.

[40] G. Beamson, D. Briggs, *High Resolution XPS of Organic Polymers: The Scienta ESCA300 Database*, Wiley, New York **1992**.
[41] D. Sindhuja, M. Gopiraman, P. Vasanthakumar, N. Bhuvanesh, R. Karvembu, *J. Organomet. Chem.* **2021**, *949*, 121933.
[42] C. Christodoulou, A. Giannakopoulos, M. V. Nardi, G. Ligorio, M. Oehzelt, L. Chen, L. Pasquali, M. Timpel, A. Giglia, S. Nannarone, P. Norman, M. Linares, K. Parvez, K. Müllen, D. Beljonne, N. Koch, *J. Phys. Chem. C* **2014**, *118*, 4784.
[43] M. Giannetto, A. Pedrini, S. Fortunati, D. Brando, S. Milano, C. Massera, R. Tatti, R. Verucchi, M. Careri, E. Dalcanale, R. Pinalli, *Sens. Actuators, B* **2018**, *276*, 340.
[44] M. Tamaddondar, A. B. Foster, M. Carta, P. Gorgojo, N. B. McKeown, P. M. Budd, *ACS Appl. Mater. Interfaces* **2020**, *12*, 46756.
[45] J. M. Powers, R. M. Caddell, *Polym. Eng. Sci.* **1974**, *12*, 432.
[46] G. M. Neville, R. Jagpal, J. Paul-Taylor, M. Tian, A. D. Burrows, C. R. Bowen, T. J. Mays, *Mater. Adv.* **2022**, *3*, 8934.
[47] W. J. Hehre, W. W. Huang, *Chemistry with Computation: an Introduction to SPARTAN*, Wavefunction, Inc. **1995**.
[48] R. Tatti, L. Aversa, R. Verucchi, E. Cavaliere, G. Garberoglio, N. M. Pugno, G. Speranza, S. Taioli, *RSC Adv.* **2016**, *6*, 37982.
[49] J. Blaber, B. Adair, A. Antoniou, *Exp. Mech.* **2015**, *55*, 1105.